



# All Redox-Active 2D MXene and 0D Phosphomolybdic Acid Nanoclusters-Anchored Polypyrrole Nanotubes for High-Performance Aqueous Hybrid Supercapacitors

Ruth Stephanie,<sup>[a]</sup> Swati J. Patil,<sup>[b]</sup> Nilesh R. Chodankar,\*<sup>[b]</sup> Yun Suk Huh,<sup>[c]</sup> Young-Kyu Han,\*<sup>[b]</sup> and Tae Jung Park\*<sup>[a]</sup>

The construction of a hybrid supercapacitor (HSC) with 2D  $Ti_3C_2T_x$  MXene anode is restricted by the scarcity of promising cathode materials that can demonstrate the superior electrochemical features in protic electrolytes. To circumvent this issue, we demonstrate an innovative high-performance HSC cell in a protic electrolyte by combining a redox-active 0D phosphomolybdic acid ( $PMo_{12}$ ) nanoclusters-anchored polypyrrole nanotubes ( $PMo_{12}/PPyNT$ ) cathode against the pseudocapacitive  $Ti_3C_2T_x$  MXene anode. Decorating  $PMo_{12}$ , a Keggin-type polyoxometalates material known for their high redox activities on polypyrrole nanotubes (PPyNT) resulting in a nanocomposite

that matches the electrochemical performance of MXene in a protic electrolyte so that a high-performance HSC cell can be acquired. The gathered  $PMo_{12}/PPyNT//MXene$  HSC cell delivers the specific energy (36.1 Wh/kg) and specific power (6.66 kW/kg) superior to the state-of-the-art MXene-based supercapacitor (SC) cells. The cell also exhibits impressive coulombic efficiencies over various current densities and adequate stability over 5000 charge-discharge cycles. These results show that combining polyoxomolybdate-based cathode materials against the MXene anode can overcome the boundaries associated with the existing HSC cells.

## Introduction

Supercapacitors are becoming an alternative energy storage device for various applications in life, ranging from displays, wearables, sensors, and other electronics. As their applications are varying and leaning towards heavier consumption, improvements are pursued to acquire supercapacitors with higher energy density and power density.<sup>[1,2]</sup> Hybrid supercapacitor (HSC) is the cell type commonly being developed for high performance supercapacitors. This construction integrates the advantages of different capacitive mechanisms from different materials on each electrode, resulting in a cell with improved voltage window and capacitance which translates to an enhanced energy density, power density, and stability.<sup>[3,4]</sup> The key to acquire successful integration of such HSC device relies in the balancing of the materials properties between the two

electrodes, such as specific surface area, conductivity, and capacitance.<sup>[5–7]</sup>

There are various materials being investigated for their use in HSC cells. MXene is becoming one of the immensely investigated alternative options as anode electrodes because of their promising properties such as metal-like conductivity ( $2 \times 10^5 \text{ S m}^{-1}$ ), rich surface chemistry, chemical stability, and high capacitance under protic (e.g.,  $H_2SO_4$ ) electrolytes.<sup>[8–11]</sup> All these are by the virtue of their inherent combined properties of metal and ceramic formed by the transition metal-carbon/nitrogen bonds.<sup>[8]</sup> Its metallic conductivity combined with hydrophilicity also enables effective wetting of electrolyte and efficient electron transfer.<sup>[12]</sup> Moreover, the layered structure of MXene can provide abundant electroactive sites for ion intercalations, resulting in higher capacitance than conventional carbon-based materials.<sup>[12,13]</sup> However, the exploration of comparable and compatible material to be used as its pairing cathode electrode remains necessary to be explored.

Conducting polymers (CP), such as polypyrrole (PPy), polyaniline (PANI), and poly(3,4-ethylenedioxothiophene) (PEDOT) have been reported to be used as the positive electrode materials in HSCs.<sup>[14–18]</sup> Particularly, polypyrrole in the form of nanotubes (PPyNT) is the leading option as it has high theoretical capacity and remarkable conductivity in addition to their ease of synthesis.<sup>[19]</sup> Several studies have shown that PPyNT were successfully employed as the positive electrodes of supercapacitors with various negative electrode materials, such as activated carbon,<sup>[20]</sup> single-walled carbon nanotubes,<sup>[21]</sup>  $MnO_2$ @reduced graphene oxide,<sup>[22]</sup> and other nanocomposites of carbon-based or metal oxide-based materials.<sup>[23,24]</sup> However, the performance of the cells was not fulfilling to their potential because it is very difficult to achieve balanced electrode

[a] R. Stephanie, Prof. T. J. Park  
Department of Chemistry, Research Institute of Chem-Bio Diagnostic Technology  
Chung-Ang University, Seoul 06974, Republic of Korea  
E-mail: tjkpark@cau.ac.kr

[b] Dr. S. J. Patil, Dr. N. R. Chodankar, Prof. Y.-K. Han  
Department of Energy and Material Engineering  
Dongguk University-Seoul  
Seoul 04620, Republic of Korea  
E-mail: chodankarnilesh@dongguk.edu  
ykenergy@dongguk.edu

[c] Prof. Y. S. Huh  
Department of Biological Engineering  
Inha University  
Incheon, 22212, Republic of Korea

Supporting information for this article is available on the WWW under  
<https://doi.org/10.1002/batt.202200108>

performance. The PPyNT-based electrode which serves as the cathode usually has lower capacitance or less surface area than the anode. Although this can somehow be fixed by charge-balancing or mass-balancing, this will not be beneficial for the long-term stability and the final energy density and power density. This issue overall leads to rapid cell performance deterioration, creating a cell with lower energy density, power density and stability.<sup>[25,26]</sup> Nano-compositing them with a highly redox-active material, such as polyoxometalates, is one of the strategies that can be used as they can provide abundant active sites for electrochemical reactions that can elevate the capacitance of the electrode.<sup>[27]</sup> One of the option is Keggin-type polyoxometalates, such as phosphomolybdic acid (PMo<sub>12</sub>), and they also have been reported to exhibit excellent redox activity in positive potential under H<sub>2</sub>SO<sub>4</sub> electrolyte.<sup>[28]</sup> In addition, they also perform the redox reactions without losing their structural integrity, which guarantees improvement for the resulting conducting polymers nanocomposite.<sup>[5,28]</sup> A study reported that decorating PPyNT with PMo<sub>12</sub> can increase the capacitive performance of almost 1.5 times compared to the bare PPyNT.<sup>[29]</sup> Such improvement then makes the nanocomposite promising to be paired with MXene to overcome the performance limitation of the HSC cell so that a cell with higher energy density and power density can be acquired.

This work demonstrates the development of an HSC cell where phosphomolybdic acid-decorated polypyrrole nanotube, named PMo<sub>12</sub>/PPyNT, is used as the cathode and Ti<sub>3</sub>C<sub>2</sub>T<sub>x</sub> MXene as the anode where aqueous H<sub>2</sub>SO<sub>4</sub> is used as the electrolyte. The PMo<sub>12</sub>/PPyNT//MXene HSC cell was demonstrated to have improved performance with 1.4 V as the optimized working voltage. On top of that, the cell also exhibits excellent maximum energy density and power density of 36.1 Wh/kg and 6.66 kW/kg, respectively, superior to other state-of-the-art MXene-based HSC cells. A series connection of two PMo<sub>12</sub>/PPyNT//MXene cells was also demonstrated to be capable of lighting up a standard red light emitting diode (LED), signifying their potential real-life application.

## Results and Discussion

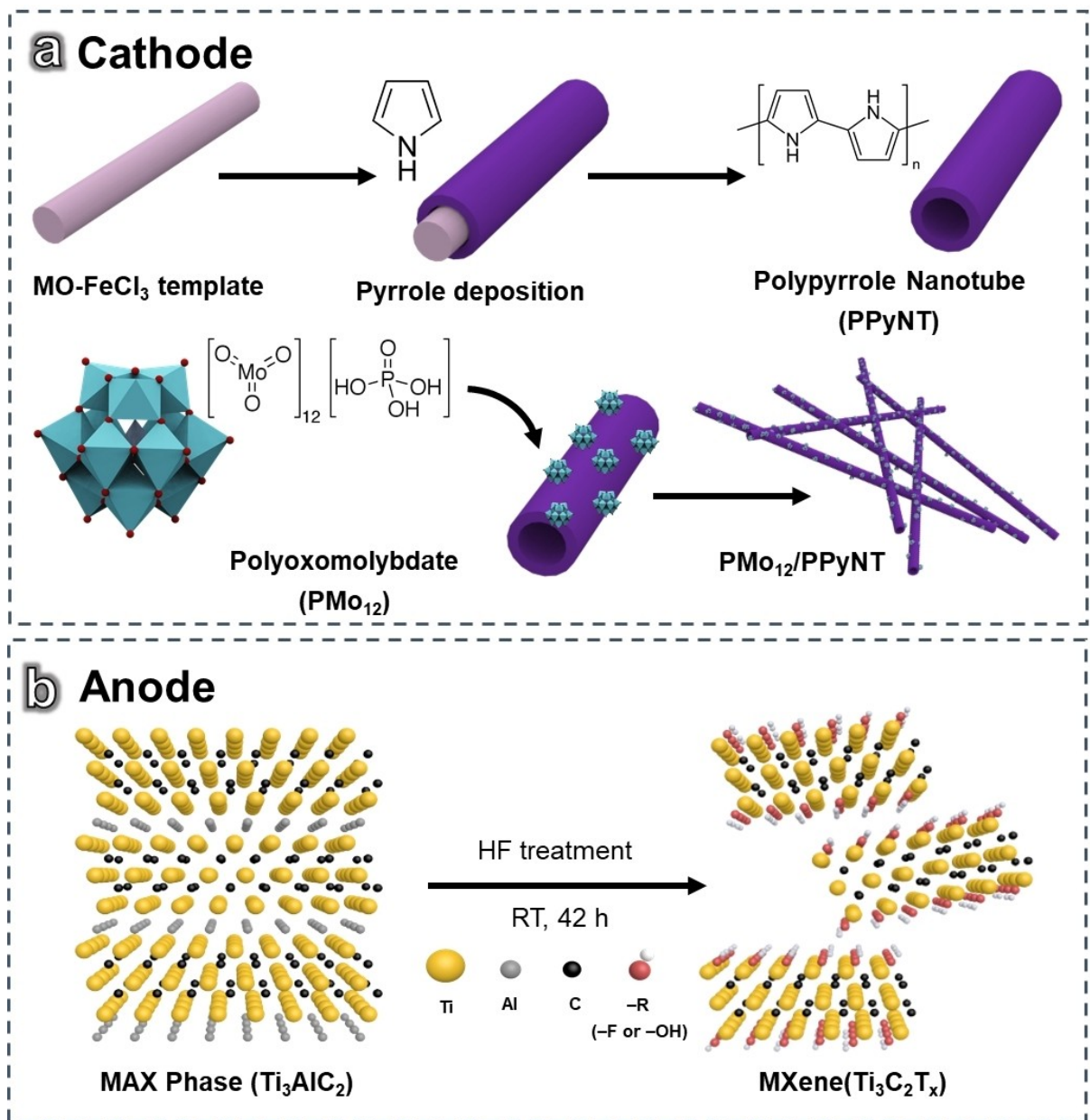
### Materials synthesis and characterization

As the electrode materials, PMo<sub>12</sub>/PPyNT and MXene are synthesized according to Scheme 1. The detailed synthesis procedures are explained in Supporting Information. In the preparation of PMo<sub>12</sub>/PPyNT (Scheme 1a), bare PPyNT was priorly synthesized through a hard-template assisted method.<sup>[29]</sup> After mixing methyl-orange (MO) with iron chloride (FeCl<sub>3</sub>), flocculates of MO–FeCl<sub>3</sub> complex were formed as microneedles and act as the sacrificial template. Upon pyrrole addition, FeCl<sub>3</sub> will act as the oxidant for pyrrole, providing nucleation site for initial polymerization resulting in the growth of tubular form along the axis of the microneedles.<sup>[30,31]</sup> This then leaves the remaining MO assemblies which can be washed out with ethanol and water continuously. Afterwards, the PPyNT is decorated with polyoxomolybdate through simple

dissociation and reduction of phosphomolybdic acid (H<sub>3</sub>PMo<sub>12</sub>O<sub>40</sub>) in water. The dissociation of phosphomolybdic acid produces PMo<sub>12</sub>O<sub>40</sub><sup>3-</sup> anions, which is a strong oxidation agent so that upon interaction with the π-electrons on the PPyNT polymer backbone, it is reduced on the PPyNT walls as ultrafine nanodots.<sup>[32,33]</sup> On the other hand, MXene is prepared through a typical wet-etching method where HF is being used to selectively etch the Al layer from the MAX phase.<sup>[5,12,13]</sup> This procedure then creates MXene with a rich functional groups on their surface, comprising of –F or –OH groups.<sup>[34]</sup> These functional groups then contribute to the efficient electrolyte wettability during electrode-electrolyte interaction, resulting in effective ion transports into the interlayers of the MXene material.

The as-prepared MXene material was then observed through scanning electron microscopy (SEM) (Figure 1a, b) and transmission electron microscopy (TEM) (Figure 1c). The SEM images reveals that the MXene sample has layered structure indicating the removal of Al layer from the MAX phase. This typical layered structure of MXene offers large electroactive sites to facilitate effective ion transports into its interlayers, making them suitable for energy applications. A detailed energy-dispersive X-ray spectroscopy (EDS) (Figure S1a, b) also reveals the chemical composition of the MXene sample, where the Al content is considerably low. The TEM image reveals the crystalline structure of the MXene with lattice distance of 1.27 nm which can be ascribed to the characteristic (002) facets of the MXene sheets.<sup>[35,36]</sup> XRD spectra were also collected and compared between the MAX phase and the as-synthesized MXene (Figure S1c). The spectra reveals that the characteristic peaks of MAX phase within the range of 33° to 43° are diminished.<sup>[37]</sup> Most importantly, the elimination of (104) diffraction peak at 2θ of 39° marks the exhaustion of Ti<sub>3</sub>AlC<sub>2</sub> as it was entirely converted to Ti<sub>3</sub>C<sub>2</sub>T<sub>x</sub>, confirming that the MXene formation was effective.<sup>[38]</sup> X-ray photoelectron spectroscopy (XPS) analyses were also performed (Figure S1d–g), revealing major peaks of Ti 2p, O 1s, F 1s, and C 1s with the atomic percentage of 20.23%, 18.11%, 16.91% and 39.48%, respectively. The concentration of oxygen (from the hydroxyl group) and fluorine functional groups were considerably high. This is desirable as they are functional groups with negative polarity which can easily bind with protons, making the MXene surface suitable for the use in H<sub>2</sub>SO<sub>4</sub> electrolyte. Minor Al 2p peaks were also observed which suggests that the remaining Al is in the form of Al<sub>2</sub>O<sub>3</sub> or AlF<sub>3</sub> as they react with HF during the synthesis and cannot be completely removed.<sup>[39]</sup>

The resulting PMo<sub>12</sub>/PPyNT material was also observed through SEM (Figure 1d, e). The morphology of the nanotube is revealed to be smooth surfaced without branches. The inner and outer diameter of the nanotube is around 70 nm and 140 nm, respectively, as revealed from the TEM image (Figure 1f). Moreover, Brunauer-Emmett-Teller (BET) analysis of nitrogen adsorption-desorption isotherm was also performed for the PMo<sub>12</sub>/PPyNT material (Figure S2a). Their BET surface area is revealed to be 20.4 m<sup>2</sup>/g with broad pore size distribution in the range of 50–120 nm (Figure S2a, inset), which is similar to other studies.<sup>[40–42]</sup> This well-defined nano-



Scheme 1. Synthesis approach of a)  $\text{PMo}_{12}/\text{PPyNT}$  and b)  $\text{Ti}_3\text{C}_2\text{T}_x$  MXene for the electrode materials.

tube form of the  $\text{PMo}_{12}/\text{PPyNT}$  nanocomposite is important not only because it results in a large surface area, but this also enables higher charge transfer rates.<sup>[19,30]</sup> In the context of PPy material itself, having nanotube form means that it has a higher proportion of ordered polymer chains, leading to longer conjugation length between the  $\pi$ -electrons and N-atoms on its backbone.<sup>[19]</sup> Anchoring the highly redox-active  $\text{PMo}_{12}$  then obviously becomes even more beneficial as it can facilitate even higher charge transport rate within the material, making them suitable for energy-oriented application.<sup>[27,43]</sup> The decoration of  $\text{PMo}_{12}$  was observed from the comparison of EDS analysis between bare PPyNT and  $\text{PMo}_{12}/\text{PPyNT}$ . The elemental mapping of PPyNT shows no presence of P and Mo element (Figure 1g), whilst on the  $\text{PMo}_{12}/\text{PPyNT}$  material,  $\text{PMo}_{12}$  are

distributed evenly throughout the PPyNT (Figure 1h, Figure S2b). XPS analyses were also performed to confirm this evidence (Figure 1i, j). The broad-scan XPS spectrum of  $\text{PMo}_{12}/\text{PPyNT}$  (Figure S2c, d) revealed the major peaks of C, O, Mo, and P. A peak of S also occurred which attributes to the remaining MO that could not be washed out completely. The narrow-scan XPS spectra of Mo 3d (Figure 1i) showed two major peaks at the binding energies of 233.02 eV (Mo 3d<sub>5/2</sub>) and 236.13 eV (Mo 3d<sub>3/2</sub>) confirming the presence of Mo with oxidation state of +6.<sup>[29]</sup> Narrow-scan XPS spectrum of P 2p (Figure 1j) revealed one major peak at the binding energy of 134.12 eV, indicating the presence of P with the oxidation state of +5.<sup>[5]</sup>

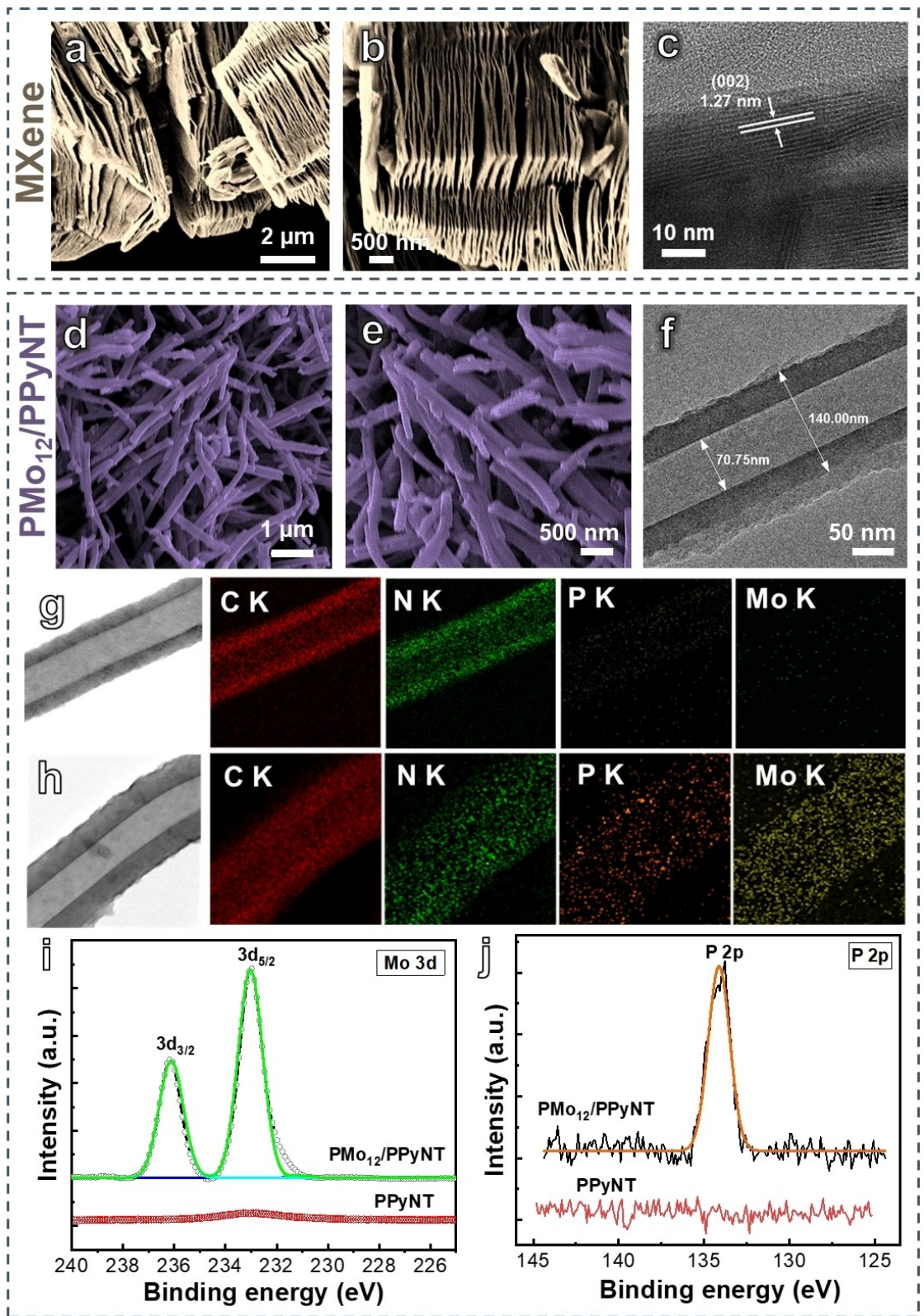


**Figure 1.** a, b) SEM images and c) TEM image of MXene, d, e) SEM images and f) TEM image of PMo<sub>12</sub>/PPyNT. EDS elemental mapping images for g) PPyNT and h) PMo<sub>12</sub>/PPyNT. Comparison of narrow-scan XPS spectra of i) Mo 3d and j) P 2p for PPyNT and PMo<sub>12</sub>/PPyNT sample.

**Half-cell electrochemical measurements**

The synthesized materials were then loaded on carbon cloth (CC) to prepare them as electrodes for electrochemical measurements and HSC cell construction. CC is chosen as the substrate because of its flexibility, high electrical conductivity, and chemical inertness, making them suitable to construct a flexible HSC cell. Prior to the full HSC cell construction, the suitability of each material to be used as electrodes was investigated by half-cell measurements through three-electrode setup. The electrolyte being used was 1 M H<sub>2</sub>SO<sub>4</sub>, Pt plate as a counter electrode, Ag/AgCl as a reference electrode, and the

MXene- or PMo<sub>12</sub>/PPyNT-loaded CC were used as the working electrode.

The cyclic voltammetry (CV) profile of the MXene electrode under various scan rate is depicted in Figure 2(a). The CV curve of MXene shows that it works well under the negative potential within the range of -0.7–0.2 V vs. Ag/AgCl, without any sign of gas evolutions. The CV curve profile is also the typical distorted rectangular shape, indicating their typical pseudocapacitive kinetics under acidic electrolyte.<sup>[9,11,44]</sup> Galvanostatic charge-discharge (GCD) measurement were also performed under various current densities, revealing distorted triangular shape with no potential drop (Figure S3a) and the calculated

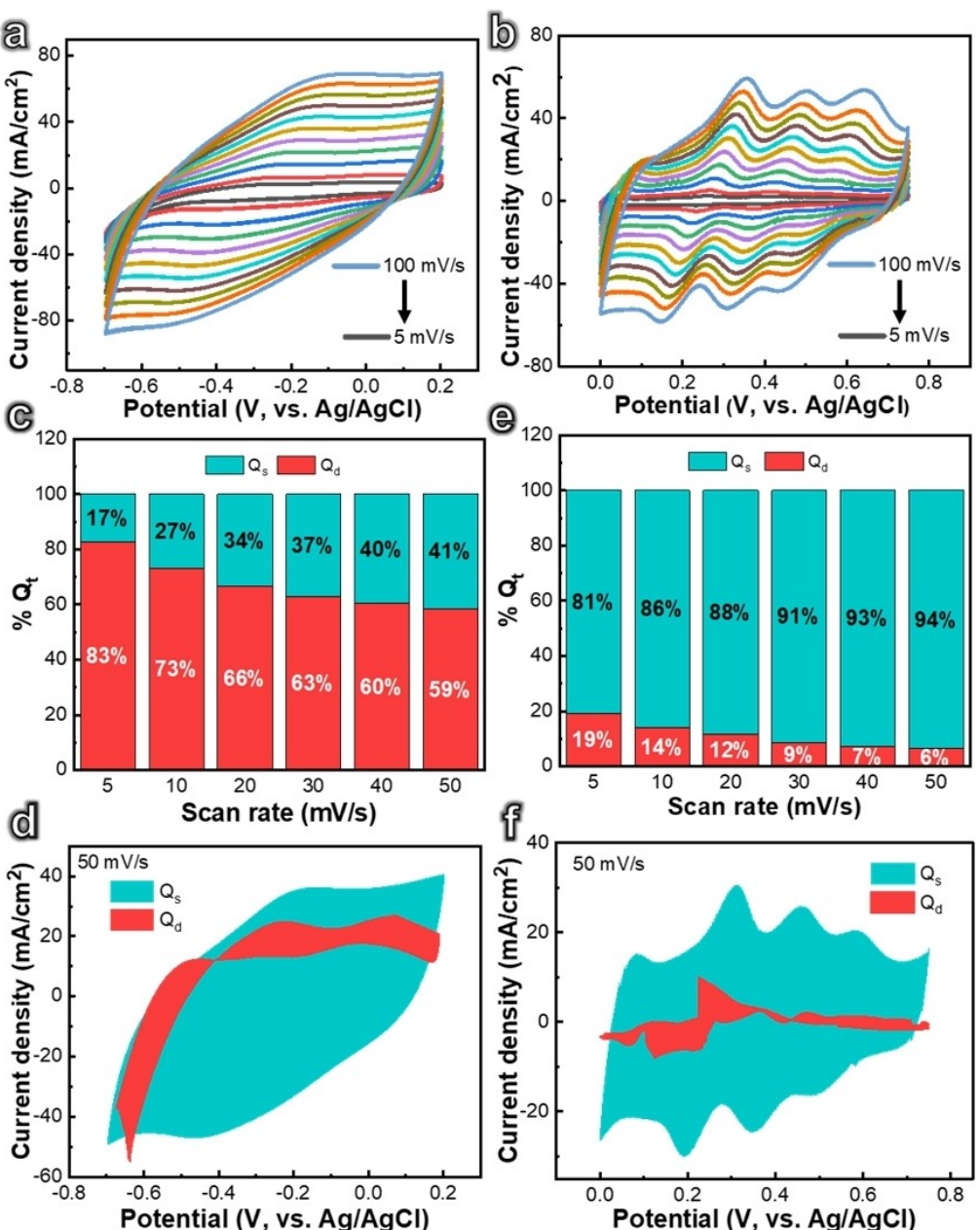
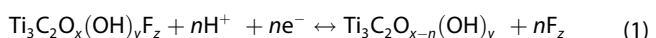
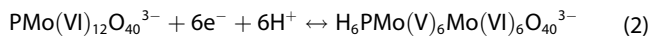


**Figure 2.** CV curves for a) MXene and b) PMo<sub>12</sub>/PPyNT electrodes at various scan rates. c) The capacitive ( $Q_s$ ) and diffusion-controlled contribution ( $Q_d$ ) of the MXene electrode and d) the representative CV curve. e) The capacitive ( $Q_s$ ) and diffusion-controlled contribution ( $Q_d$ ) of the PMo<sub>12</sub>/PPyNT electrode and f) the representative CV curve. Both voltammetry responses are compared at the scan rate of 50 mV/s. The red-colored CV curves indicates the contribution of  $Q_d$ .

coulombic efficiency (Figure S3b) showed excellent values. The calculated maximum capacitance of the MXene electrode is 401.05 F/g at 8.3 A/g current density. The reaction which occurs during the electrochemical energy storing process of the MXene is shown in reaction (1).



The CV profiles of the  $\text{PMo}_{12}/\text{PPyNT}$  electrode is depicted in Figure 2(b). It is shown to work stably under the positive voltage, ranging from 0–0.75 V without any sign of gas evolutions. The profile of the CV curves are also shown to have multiple peaks consistently, attributable to the redox peaks of PPyNT and the redox activities of  $\text{PMo}_{12}$ .<sup>[5,19,27,32]</sup> The performance of bare PPyNT and  $\text{PMo}_{12}/\text{PPyNT}$  were also compared through CV and GCD (Figure S4a and b, respectively). The result shows that  $\text{PMo}_{12}/\text{PPyNT}$  is better than bare PPyNT as it has wider CV profile at the same scan rate. It also has higher discharge time, all of which translates to better capacitance. The GCD measurements and coulombic efficiency calculation for the  $\text{PMo}_{12}/\text{PPyNT}$  electrode are plotted under Figure S5a and S5b, respectively, showing distorted triangular profile without potential drop and with desirable coulombic efficiency under various current densities. The maximum capacitance of the  $\text{PMo}_{12}/\text{PPyNT}$  electrode is 386.67 F/g at 2.04 A/g current density. The total electrochemical reactions that occurred for the  $\text{PMo}_{12}/\text{PPyNT}$  nanocomposites are comprised of two main reactions for both materials, presented in reaction (2) for  $\text{PMo}_{12}$  and Scheme 2 for the PPyNT. The electrochemical activities of  $\text{PMo}_{12}$  are attributed to three constructive redox reactions that occur with two-electron transfer process for each.<sup>[5,32]</sup> On the other hand, the electrochemical behavior of PPyNT is related to the anion transport in and out of the polymer backbone.<sup>[45]</sup>



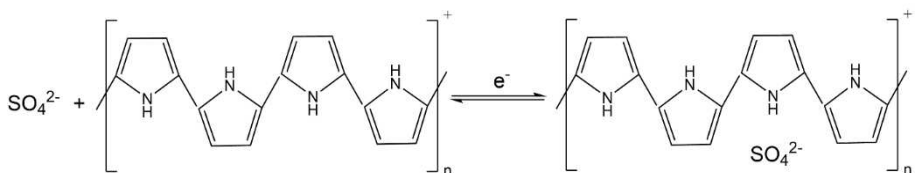
To further understand the charge storing kinetics of both electrodes, the contributions of the capacitive and diffusion effects to the total charge stored were analyzed according to Dunn and Lu's method.<sup>[46]</sup> The total current response ( $Q_t$ ) of an electrode collected from CV measurements is the combination of two separate mechanisms: surface charge ( $Q_s$ ) and diffusion-controlled charge ( $Q_d$ ), which follows Equation (3).

$$Q_t = Q_s + Q_d \quad (3)$$

The value of  $Q_s$  is attributable with the contribution of fast kinetic reactions, including electrical double-layer charge and

faradaic redox activity induced charge. This value is not dependent on the scan rate. Whilst the value of  $Q_d$  is attributed with slow kinetic reaction, typically ion migrations into the interlayer of the nanomaterials. The results are shown in Figure 2(c) for the MXene electrode and Figure 2(e) for the  $\text{PMo}_{12}/\text{PPyNT}$  electrode. Total charges ( $Q_t$ ) at different scan rates are represented by the overall bars, while the green and red parts represent  $Q_s$  and  $Q_d$ , respectively. The result of the capacitive contributions of MXene electrode at several scan rates is depicted in Figure 2(c), and the representative CV curve is shown in Figure 2(d). For the MXene electrode, it is shown that the fraction of  $Q_d$  is dominant at most scan rates. The value of  $Q_d$  is attributed to diffusion-controlled charge storing mechanism, typically the intercalation of ions into the layers of the material.<sup>[47]</sup> This suggests that the prominent process on the MXene electron is ion intercalations onto its layers. On the other hand, the result of the capacitive contributions of  $\text{PMo}_{12}/\text{PPyNT}$  electrode at several scan rates is depicted in Figure 2(e), and the representative CV curve is shown in Figure 2(f). In contrast to MXene, the calculated capacitive contribution for the  $\text{PMo}_{12}/\text{PPyNT}$  electrode is majorly fractioned to  $Q_s$ , which value is attributed to the surface capacitive process.<sup>[46–48]</sup> This surface capacitive process includes fast kinetic reactions such as faradaic redox-activities, in this case can be attributed to the high activity of the abundant  $\text{PMo}_{12}$  decorated onto the PPyNT. The role of  $\text{PMo}_{12}$  in enhancing the supercapacitive performance of PPyNT is also revealed by comparing the ratio of  $Q_s$  and  $Q_d$  in bare PPyNT, as shown in Figure S6. The results showed that bare PPyNT has a lower  $Q_s$  contribution than  $\text{PMo}_{12}/\text{PPyNT}$ . Comparing their  $Q_s$  and  $Q_d$  contributions reveals that the  $Q_s$  contribution was increased by up to 13%, emphasizing the importance of  $\text{PMo}_{12}$  decoration to increase the electrochemical activity of the  $\text{PMo}_{12}/\text{PPyNT}$  electrode that benefits their supercapacitive performance.

These dissimilarities between MXene and  $\text{PMo}_{12}/\text{PPyNT}$  as electrode materials then becomes very beneficial for HSC cell construction. Firstly, their operating potential windows are complementary, where MXene works on the negative and  $\text{PMo}_{12}/\text{PPyNT}$  on the positive potential. Combining them as one HSC cell then results in a device with wide voltage window that helps to achieve a higher energy density. Secondly, their differing charge storage mechanisms are obviously beneficial for the total device constructions. By combining the two dissimilar electrodes, the advantages of both mechanisms are integrated into device, creating a cell with improved capacitance which translates to higher energy density, along with improved power density and stability. The dissimilarity in their majoring charge storing mechanisms is also an important



Scheme 2. Electrochemical behavior of PPy in 1 M  $\text{H}_2\text{SO}_4$ .

aspect that defines them to be within the class of hybrid supercapacitor cells.

### Full cell measurements

The schematic of the  $\text{PMo}_{12}/\text{PPyNT} // \text{MXene}$  HSC cell construction is depicted in Figure 3(a). As confirmed in their half-cell studies, MXene was used as the anode and  $\text{PMo}_{12}/\text{PPyNT}$  was used as the cathode to assemble the HSC cell. Prior to the assembly, all electrodes and separator were soaked in 1 M  $\text{H}_2\text{SO}_4$  for 2 h, before lastly parafilm was used to mantle the whole HSC cell. Mass balancing was also performed to balance the charges on both electrodes prior to the assembly of the HSC cell (Supporting Information). The calculated optimized mass ratio between  $\text{PMo}_{12}/\text{PPyNT}$  and MXene electrodes was 1:1.03, and the total mass loading was  $2.1 \text{ mg/cm}^2$ .

Generally, the voltage window of the HSC cell can be determined from the voltage windows of the respective materials. Figure 3(b) shows the respective potential windows for the MXene and  $\text{PMo}_{12}/\text{PPyNT}$  electrodes at the constant scan rate of 50 mV/s in the three-electrode setup. However, optimizations should be performed to get a device with not only desirable voltage window but also with desirable energy density and stability.<sup>[7]</sup> The optimization was performed by

checking the charge-discharge performance of the HSC cell under various voltage window, which result is depicted in Figure 3(c). The CV profiles of the cell under different potential windows were also collected and plotted in Figure S7(a). The results showed that the cell might work up to 1.7 V, but the coulombic efficiency will be low despite its higher capacitance. Under 1.5 V, the charge-discharge curve also suggested that the cell can work well, but probably this will not create a stable device as it is working right on its limits. Having the cell to work under 1.3 V is certainly able to make a device with much better stability, but the acquired capacitance will not be fulfilling to its potential, which will lead to a lesser energy density. The relationship of the capacitance and coulombic efficiency of each performance under the various voltage window was then calculated and plotted under Figure S7(b), where the intersection of high capacitance with desirable stability can be acquired by choosing 1.4 V as the voltage window. Hence, further HSC cell measurements were done using 1.4 V as the voltage window.

The charge-discharge performance of the cell is then measured under various current densities (Figure 4a) and the CV profiles under different scan rates are plotted in Figure S7(c). The charge-discharge profile reveals distorted triangular shape without voltage drop accompanied with consistent increments of the charge-discharge time. This suggests that the optimized

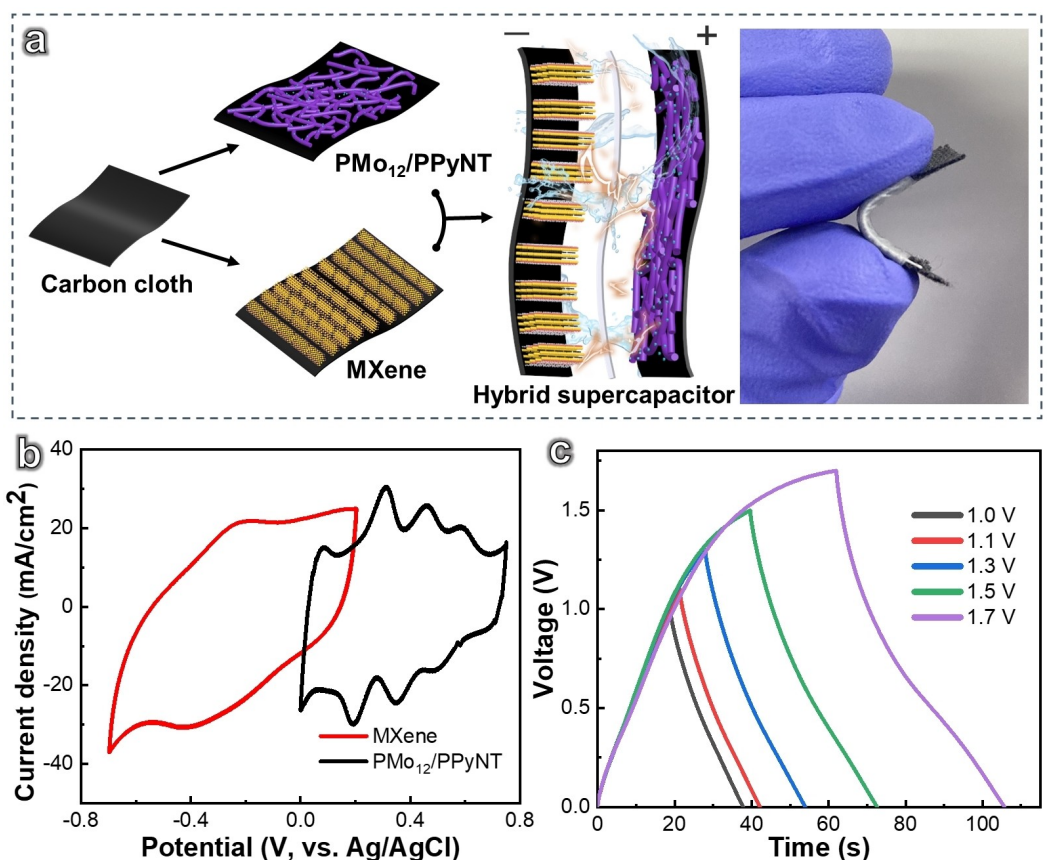


**Figure 3.** a) Schematic figure of the  $\text{PMo}_{12}/\text{PPyNT} // \text{MXene}$  HSC cell construction and the real picture. b) CV curves depicting potential window of MXene and  $\text{PMo}_{12}/\text{PPyNT}$  electrodes (Scan rate: 50 mV/s). c) Charge-discharge curve for  $\text{PMo}_{12}/\text{PPyNT} // \text{MXene}$  HSC cell voltage window optimization (Current density: 5.7 A/g).

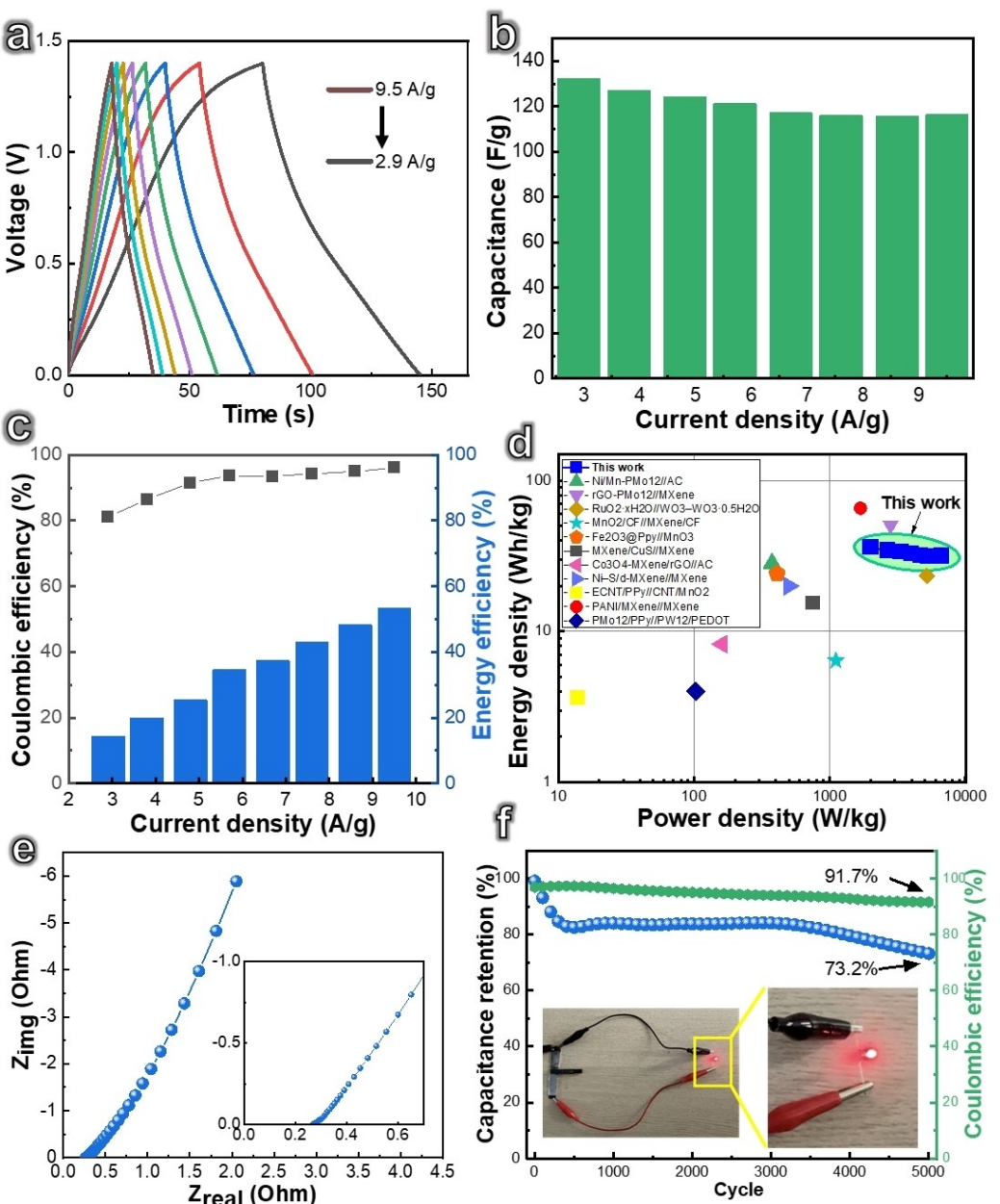


**Figure 4.** a) Charge-discharge curves for the  $\text{PMo}_{12}/\text{PPyNT}/\text{MXene}$  HSC cell at several voltage windows. b) Capacitance, c) coulombic efficiency and energy density of the  $\text{PMo}_{12}/\text{PPyNT}/\text{MXene}$  HSC cell. d) Ragone plot for the  $\text{PMo}_{12}/\text{PPyNT}/\text{MXene}$  HSC cell. e) Nyquist plot of the  $\text{PMo}_{12}/\text{PPyNT}/\text{MXene}$  HSC cell. f) Stability test results for the  $\text{PMo}_{12}/\text{PPyNT}/\text{MXene}$  HSC cell for 5000 cycles at 11.9 A/g and the respective coulombic efficiency. (inset: a connection of two  $\text{PMo}_{12}/\text{PPyNT}/\text{MXene}$  cells in series can light up a red LED).

mass balancing is acquired, along with good electrical conductivity of the electrodes beneficial for the power performance of the HSC cell. The capacitance under various current densities is depicted under Figure 4(b) with the maximum value of 132.5 F/g at 2.9 A/g current density. Moreover, the gentle increment of the capacitance values under various current densities depicts the good capacitance retention of the cell. At elevated current density of 9.5 A/g, the calculated capacitance is 116.33 F/g, yielding excellent capacitance retention value of 87.8%. This demonstrates the excellent energy storage capability of the HSC cell to operate under wide conditions, which is beneficial for real-life applications.

In practical, not only energy density but also desirable coulombic and energy efficiencies are required to minimize the device maintenance cost. Hence, the relationship between the coulombic efficiency and energy efficiency of the  $\text{PMo}_{12}/\text{PPyNT}/\text{MXene}$  cell under various current densities is furtherly calculated and plotted in Figure 4(c). The coulombic efficiencies are excellent under all current densities with the lowest value of 81.8% at 2.9 A/g. The coulombic efficiency even reached a noteworthy maximum value of 96.1% at 9.5 A/g. The increment of coulombic efficiency at elevated current density is ruled by the fact that the prominent occurring reactions will differ depending on the applied current density. At a higher current

density, the surface of the electrode becomes more active so that the energy barrier which must be overcome by charges in moving from the electrolyte towards the electrode is lower. This facilitates the fast electrical double-layer capacitive behavior to be prominent, leading to an increased coulombic efficiency.<sup>[49,50]</sup> On the other hand, lowering the current density allows the slower pseudocapacitive redox reaction to take place, giving rise to internal resistance, decreasing the power capability of the cell, which results in the decrement of coulombic efficiency to some degree.<sup>[50,51]</sup> In regard of the energy efficiency of the cell, it is only desirable starting from 7.6 A/g current density where it starts to show the value above 40%. The lower energy efficiency under lower current density is inevitable as slow reactions begin to be prominent, leading to polarization energy losses as the share of current going to the electrochemical reaction is increased.<sup>[52]</sup>

The specific energy and specific power of the HSC cell are then calculated and plotted in the Ragone plot and compared with MXene and PMo<sub>12</sub>-based asymmetric and HSC cells (Figure 4d, Table 1). The PMo<sub>12</sub>/PPyNT//MXene HSC cell acquired specific energy of 31.67 Wh/kg at maximum 6666.67 W/kg specific power. At lower current density of 2.5 A/g, the cell reaches maximum 36.1 Wh/kg specific energy at 2000 W/kg specific power. As shown in Figure 4(d), the PMo<sub>12</sub>/PPyNT//MXene HSC cell is superior to most of MXene- or PPyNT-based HSC cells. Moreover, it is also better than some of the well-established materials such as Ni-based or MnO<sub>2</sub>-based supercapacitors (Table 1). The high specific energy and power are obviously desirable for real-life applications as it translates to a longer duration in using the device while the recharging time is shortened, respectively.

The impedance of the PMo<sub>12</sub>/PPyNT//MXene HSC cell was analyzed through electrochemical impedance spectroscopy (EIS) analysis. The result is plotted in the form of Nyquist plot (Figure 4e). The collective resistance (ESR) is determined using the first intercept of the Nyquist plot in high-frequency region. This ESR value is the total resistance of the current collector, electrode materials, and electrolyte which were determined to

be in a low value of 0.27 Ω/cm<sup>2</sup>. The Nyquist plot also showed the absence of a semi-circle which confirms the high conductivity of the HSC cell. This confirms the efficient interaction between the electrodes and the electrolytes by the virtue of the good electrical conductivity of the electrode materials along with the high ionic conductivity of the electrolyte. This environment translates to effective ion transport that benefits the power performance of the cell which is proven by the excellent specific power of 6666.67 W/kg.

The stability test of the PMo<sub>12</sub>/PPyNT//MXene HSC cell was performed through charge-discharge test for 5000 cycles. The corresponding capacitance retention and coulombic efficiency of the PMo<sub>12</sub>/PPyNT//MXene HSC cell are shown in Figure 4(f). The result shows that after 500 cycles, it dropped significantly to 83.7%. According to a previous study, this steep drop is a result of structural pulverization of PPyNT due to the repeated volumetric swelling and shrinking, especially at initial stages.<sup>[26]</sup> However, after some degree, the stability can be maintained as PPyNT is abundantly decorated with the PMo<sub>12</sub> which is known to perform well without losing its structural integrity. These fine decoration of PMo<sub>12</sub> on the PPyNT then accommodate the effect of the volumetric expansion to alleviate the structural pulverization effect. As a result, 73.2% of its initial capacitance was still retained even after 5000 cycles of charging and discharging at 11.9 A/g. This issue can be fixed by furtherly nanocompositing the PPyNT with another mechanically stable nanomaterial such as graphene, siloxane, or other metallic nanomaterials before decorating them with PMo<sub>12</sub>, which will be done in our future works. On another note, the coulombic efficiency of the device is also presented in Figure 4f that shows the value of above 90% during the whole stability test. At the 5000<sup>th</sup> cycle, an excellent value of 91.7% of coulombic efficiency was still maintained. Finally, two PMo<sub>12</sub>/PPyNT//MXene HSC cells were connected in series which capable to light up a red light-emitting diode (Figure 4f), signifying their potential real-life application.

**Table 1.** Comparison of electrochemical parameters and performances of this work with other similar materials based on hybrid or asymmetric configuration.

Cathode	Anode	Electrolyte	Voltage window [V]	Maximum specific energy [Wh/kg]	Maximum specific power [W/kg]	Ref.
PMo <sub>12</sub> /PPyNT	MXene	1 M H <sub>2</sub> SO <sub>4</sub>	1.4	36.1	6666.67	This work
Fe <sub>2</sub> O <sub>3</sub> @PPy	MnO <sub>2</sub>	1 M Na <sub>2</sub> SO <sub>4</sub>	2.0	24.2	408.2	[53]
rGO-PMo <sub>12</sub>	MXene	1 M H <sub>2</sub> SO <sub>4</sub>	1.4	50.46	7000	[5]
MnO <sub>2</sub> /CF	MXene/CF	PVA-1 M H <sub>2</sub> SO <sub>4</sub>	1.5	6.4	1107.7	[54]
rGO@PPy	MXene	3 M H <sub>2</sub> SO <sub>4</sub>	1.45	16	200	[55]
PMo <sub>12</sub> /PPy	PW <sub>12</sub> /PEDOT	0.5 M H <sub>2</sub> SO <sub>4</sub>	1.0	4	103	[56]
Ni/Mn-PMo <sub>12</sub>	Activated carbon	3 M KOH	1.5	28.3	375	[57]
PANI/MXene	MXene	1 M H <sub>2</sub> SO <sub>4</sub>	1.4	65.6	1687.3	[15]
ECNT/PPy	CNT/MnO <sub>2</sub>	5M LiCl	1.9	3.63	13.86	[58]
MXene/CuS	MXene	1 M KOH	1.5	15.4	750.2	[59]
Ni-S/d-MXene	d-MXene	6 M KOH	1.9	20	500	[60]
RuO <sub>2</sub> ·xH <sub>2</sub> O	WO <sub>3</sub> ·WO <sub>3</sub> ·0.5H <sub>2</sub> O	0.5 M H <sub>2</sub> SO <sub>4</sub>	1.6	23.4	5200	[61]
Co <sub>3</sub> O <sub>4</sub> -MXene/rGO	Activated carbon	6 M KOH	1.6	8.25	159.94	[62]
PPy/PMA	PEDOT/PTA	0.5 M H <sub>2</sub> SO <sub>4</sub>	1	4	103	[63]
{Mo <sub>132</sub> }/rGO	Modified AC	1 M Li <sub>2</sub> SO <sub>4</sub>	2.1	31.6	207.7	[64]
PV <sub>4</sub> W <sub>8</sub> -PPy	PPy	0.5 M H <sub>2</sub> SO <sub>4</sub>	0.8	16.4	756.78	[65]

## Conclusion

This work demonstrates the development of a high-performance HSC cell by using  $Ti_3C_2T_x$  MXene and  $PMo_{12}/PPyNT$  as the anode and cathode electrode materials, respectively. The  $PMo_{12}/PPyNT//MXene$  HSC cell reaches specific energy of 31.67 Wh/kg at maximum 6.6 kW/kg specific power. At a lower current density, the cell reaches maximum 36.1 Wh/kg specific energy at 2000 W/kg specific power. The superior performance is attributed to the synergistic charge storing and discharging mechanism by the hybrid configuration of the electrode materials with balanced properties. MXene contributes to the high performance by the nature of its layered structure, enabling effective electrolyte transport into its interlayer spaces. On the other hand,  $PMo_{12}/PPyNT$  contributes effectively to the charge storing mechanism by the virtue of the highly redox active  $PMo_{12}$  abundantly being decorated on the inherently pseudocapacitive PPyNT. The stability test also revealed that the HSC cell can retain more than 73% of its initial capacitance even after 5000 cycles of charging and discharging, while still maintaining 91.7% of coulombic efficiency at the final cycle. A series connection of two  $PMo_{12}/PPyNT//MXene$  HSC cells is also demonstrated to be capable of lighting up a red LED, signifying their potential real-life application.

## Appendix A. Supplementary Data

Supporting Information is available from the Wiley Online Library or from the author.

## Acknowledgements

This work is supported by the National Research Foundation of Korea (NRF) grant funded by the Ministry of Science and ICT (MSI) (NRF-2019R1A2C2084065) and the Chung-Ang University Young Scientist Scholarship (CAYSS) in 2020. This work was also supported by the Dongguk University Research Fund of 2021 (S-2021-G0001-00093).

## Conflict of Interest

The authors declare no conflict of interest.

## Data Availability Statement

The data that support the findings of this study are available from the corresponding author upon reasonable request.

**Keywords:** hybrid supercapacitor • MXene • polyoxomolybdate • polypyrrole nanotube • protic electrolyte

- [1] P. Forouzandeh, V. Kumaravel, S. C. Pillai, *Catalysts* **2020**, *10*, 969.
- [2] T. M. Gür, *Energy Environ. Sci.* **2018**, *11*, 2696–2767.
- [3] N. R. Chodankar, H. D. Pham, A. K. Nanjundan, J. F. S. Fernando, K. Jayaramulu, D. Golberg, Y.-K. Han, D. P. Dubal, *Small* **2020**, *16*, 2002806.
- [4] S. Kumar, G. Saeed, L. Zhu, K. N. Hui, N. H. Kim, J. H. Lee, *Chem. Eng. J.* **2021**, *403*, 126352.
- [5] S.-K. Hwang, S. J. Patil, N. R. Chodankar, Y. S. Huh, Y.-K. Han, *Chem. Eng. J.* **2022**, *427*, 131854.
- [6] J. Huang, K. Yuan, Y. Chen, *Adv. Funct. Mater.* **2022**, *32*, 2108107.
- [7] D. M. Sayed, M. M. Taha, L. G. Ghanem, M. S. El-Deab, N. K. Allam, *J. Power Sources* **2020**, *480*, 229152.
- [8] C. J. Zhang, B. Anasori, A. Seral-Ascaso, S.-H. Park, N. McEvoy, A. Shmeliov, G. S. Duesberg, J. N. Coleman, Y. Gogotsi, V. Nicolosi, *Adv. Mater.* **2017**, *29*, 1702678.
- [9] N. Kurra, S. Uzun, G. Valourouthu, Y. Gogotsi, *Energy Storage Mater.* **2021**, *39*, 347–353.
- [10] L. Qin, Q. Tao, A. el Ghazaly, J. Fernandez-Rodriguez, P. O. Å Persson, J. Rosen, F. Zhang, *Adv. Funct. Mater.* **2018**, *28*, 1703808.
- [11] P. Das, Z.-S. Wu, *J. Phys. E* **2020**, *2*, 32004.
- [12] X. Zang, J. Wang, Y. Qin, T. Wang, C. He, Q. Shao, H. Zhu, N. Cao, *Nano-Micro Lett.* **2020**, *12*, 77.
- [13] M. Naguib, M. W. Barsoum, Y. Gogotsi, *Adv. Mater.* **2021**, *33*, 2103393.
- [14] W. Liang, I. Zhitomirsky, *Electrochim. Acta* **2022**, *406*, 139843.
- [15] Y. Wang, X. Wang, X. Li, Y. Bai, H. Xiao, Y. Liu, G. Yuan, *Chem. Eng. J.* **2021**, *405*, 126664.
- [16] J. Yang, J. Y. Cao, Y. D. Peng, M. Bissett, I. A. Kinloch, R. A. W. Dryfe, *J. Power Sources* **2021**, *516*, 10.
- [17] P. Luan, N. Zhang, W. Zhou, Z. Niu, Q. Zhang, L. Cai, X. Zhang, F. Yang, Q. Fan, W. Zhou, Z. Xiao, X. Gu, H. Chen, K. Li, S. Xiao, Y. Wang, H. Liu, S. Xie, *Adv. Funct. Mater.* **2016**, *26*, 8178–8184.
- [18] N. Zhang, P. Luan, W. Zhou, Q. Zhang, L. Cai, X. Zhang, W. Zhou, Q. Fan, F. Yang, D. Zhao, Y. Wang, S. Xie, *Nano Res.* **2014**, *7*, 1680–1690.
- [19] J. Stejskal, M. Trchová, *Chem. Pap.* **2018**, *72*, 1563–1595.
- [20] J. Keskinen, S. Tuurala, M. Sjödin, K. Kiri, L. Nyholm, T. Flyktman, M. Strømme, M. Smolander, *Synth. Met.* **2015**, *203*, 192–199.
- [21] K. H. An, K. K. Jeon, J. K. Heo, S. C. Lim, D. J. Bae, Y. H. Lee, *J. Electrochem. Soc.* **2002**, *149*, A1058.
- [22] N. S. Arul, J. I. Han, P. C. Chen, *ChemElectroChem* **2018**, *5*, 2747–2757.
- [23] J. P. Jyothibasu, M.-Z. Chen, Y.-C. Tien, C.-C. Kuo, E.-C. Chen, Y.-C. Lin, T.-C. Chiang, R.-H. Lee, *Catalysts* **2021**, *11*, 980.
- [24] G. Shimoga, R. R. Palem, D.-S. Choi, E.-J. Shin, P.-S. Ganesh, G. D. Saratale, R. G. Saratale, S.-H. Lee, S.-Y. Kim, *Metals* **2021**, *11*, 905.
- [25] J. Parayangattil Jyothibasu, M.-Z. Chen, R.-H. Lee, *ACS Omega* **2020**, *5*, 6441–6451.
- [26] Y. Song, T.-Y. Liu, X.-X. Xu, D.-Y. Feng, Y. Li, X.-X. Liu, *Adv. Funct. Mater.* **2015**, *25*, 4626–4632.
- [27] M. R. Horn, A. Singh, S. Alomari, S. Goberna-Ferrón, R. Benages-Vilau, N. Chodankar, N. Motta, K. Ostríkov, J. Macleod, P. Sonar, P. Gomez-Romero, D. Dubal, *Energy Environ. Sci.* **2021**, *14*, 1652–1700.
- [28] N. I. Gumerova, A. Rompel, *Nat. Chem. Rev.* **2018**, *2*, 112.
- [29] D. P. Dubal, B. Ballesteros, A. A. Mohite, P. Gómez-Romero, *ChemSusChem* **2017**, *10*, 731–737.
- [30] J. Kopecká, D. Kopecký, M. Vrňata, P. Fitl, J. Stejskal, M. Trchová, P. Bober, Z. Morávková, J. Prokeš, I. Sapurina, *RSC Adv.* **2014**, *4*, 1551–1558.
- [31] M. Omastová, M. Trchová, J. Kovářová, J. Stejskal, *Synth. Met.* **2003**, *138*, 447–455.
- [32] S. Dong, W. Jin, *J. Electroanal. Chem.* **1993**, *354*, 87–97.
- [33] S. S. Ray, R. Gusain, N. Kumar, in *Carbon Nanomaterial-Based Adsorbents for Water Purification*, Elsevier, **2020**, pp. 327–340.
- [34] M. Alhabeb, K. Maleski, B. Anasori, P. Lelyukh, L. Clark, S. Sin, Y. Gogotsi, *Chem. Mater.* **2017**, *29*, 7633–7644.
- [35] H. Jiang, Z. Wang, Q. Yang, L. Tan, L. Dong, M. Dong, *Nano-Micro Lett.* **2019**, *11*, 31.
- [36] M. Naguib, M. Kurtoglu, V. Presser, J. Lu, J. Niu, M. Heon, L. Hultman, Y. Gogotsi, M. W. Barsoum, *Adv. Mater.* **2011**, *23*, 4248–4253.
- [37] W. Feng, H. Luo, Y. Wang, S. Zeng, L. Deng, X. Zhou, H. Zhang, S. Peng, *RSC Adv.* **2018**, *8*, 2398–2403.
- [38] J. Luo, W. Zhang, H. Yuan, C. Jin, L. Zhang, H. Huang, C. Liang, Y. Xia, J. Zhang, Y. Gan, X. Tao, *ACS Nano* **2017**, *11*, 2459–2469.
- [39] A. Szuplewska, D. Kulpińska, A. Dybko, A. M. Jastrzębska, T. Wojciechowski, A. Rozmysłowska, M. Chudy, I. Grabowska-Jadach, W. Ziemiowska, Z. Brzózka, A. Olszyna, *Mater. Sci. Eng. C* **2019**, *98*, 874–886.

- [40] W. Wei, Q. Wang, J. Li, D. Liu, J. Niu, P. Liu, *J. Inst. Chem.* **2021**, *129*, 135–143.
- [41] S. Budi, F. Rahmadi, S. Muhab, *J. Chem. Technol. Metall.* **2020**, *55*, 28–33, [https://cassi.cas.org/publication.jsp?P=eCQtRPJo9AQyz133K\(\(\(AMP\)\)\)&lowbar\(\(\(SEMI\)\)\)&I3zLPXfcr-WXfJmdj1To7iOyXJWPRk2w0T8-XojRRDGrzdmwAJJuwqrmbuTiwZzw2gwClAG-IfQ3gUMs9d9yv5Zd8yz133K\(\(\(AMP\)\)\)&lowbar\(\(\(SEMI\)\)\)&II39GnxBlsYQBIT-nOsFRP03w](https://cassi.cas.org/publication.jsp?P=eCQtRPJo9AQyz133K(((AMP)))&lowbar(((SEMI)))&I3zLPXfcr-WXfJmdj1To7iOyXJWPRk2w0T8-XojRRDGrzdmwAJJuwqrmbuTiwZzw2gwClAG-IfQ3gUMs9d9yv5Zd8yz133K(((AMP)))&lowbar(((SEMI)))&II31097aObglrVMs9d9yv5Zd8yz133K(((AMP)))&lowbar(((SEMI)))&II39GnxBlsYQBIT-nOsFRP03w).
- [42] J. Liu, J. An, Y. Ma, M. Li, R. Ma, *J. Electrochem. Soc.* **2012**, *159*, A828–A833.
- [43] D. Wang, L. Liu, J. Jiang, L. Chen, J. Zhao, *Nanoscale* **2020**, *12*, 5705–5718.
- [44] X. Ji, K. Xu, C. Chen, B. Zhang, Y. Ruan, J. Liu, L. Miao, J. Jiang, *Phys. Chem. Chem. Phys.* **2016**, *18*, 4460–4467.
- [45] A. F. Diaz, J. I. Castillo, J. A. Logan, W.-Y. Lee, *J. Electroanal. Chem. Interfacial Electrochem.* **1981**, *129*, 115–132.
- [46] Z. Chen, V. Augustyn, X. Jia, Q. Xiao, B. Dunn, Y. Lu, *ACS Nano* **2012**, *6*, 4319–4327.
- [47] S. D. Perera, X. Ding, A. Bhargava, R. Hovden, A. Nelson, L. F. Kourkoutis, R. D. Robinson, *Chem. Mater.* **2015**, *27*, 7861–7873.
- [48] J. Wang, J. Polleux, J. Lim, B. Dunn, *J. Phys. Chem. C* **2007**, *111*, 14925–14931.
- [49] W. Plieth, in *Electrochemistry for Materials Science*, Elsevier, Amsterdam, **2008**, pp. 169–193.
- [50] M. Rajkumar, C.-T. Hsu, T.-H. Wu, M.-G. Chen, C.-C. Hu, *Prog. Nat. Sci.* **2015**, *25*, 527–544.
- [51] S. Wang, Y. Fan, D.-I. Stroe, C. Fernandez, C. Yu, W. Cao, Z. Chen, in *Battery System Modeling*, Elsevier, **2021**, pp. 1–46.
- [52] D. A. Bograchev, D. Y. Gryzlov, V. E. Sosenkin, Y. Volkovich, *Electrochim. Acta* **2019**, *319*, 552–560.
- [53] Y. Wang, Z. Du, J. Xiao, W. Cen, S. Yuan, *Electrochim. Acta* **2021**, *386*, 138486.
- [54] Y. Wei, M. Zheng, W. Luo, B. Dai, J. Ren, M. Ma, T. Li, Y. Ma, *J. Energy Storage* **2022**, *45*, 103715.
- [55] M. Boota, Y. Gogotsi, *Adv. Energy Mater.* **2019**, *9*, 1802917.
- [56] G. M. Suppes, C. G. Cameron, M. S. Freund, *J. Electrochem. Soc.* **2010**, *157*, A1030.
- [57] M. Huang, P. Wang, Y. Liu, J. Zhao, Q. Lin, M. Lu, *Appl. Surf. Sci.* **2019**, *497*, 143760.
- [58] Z.-H. Chang, D.-Y. Feng, Z.-H. Huang, X.-X. Liu, *Chem. Eng. J.* **2018**, *337*, 552–559.
- [59] Z. Pan, F. Cao, X. Hu, X. Ji, *J. Mater. Chem. A* **2019**, *7*, 8984–8992.
- [60] Y. Luo, C. Yang, Y. Tian, Y. Tang, X. Yin, W. Que, *J. Power Sources* **2020**, *450*, 227694.
- [61] K. H. Chang, C. C. Hu, C. M. Huang, Y. L. Liu, C. I. Chang, *J. Power Sources* **2011**, *196*, 2387–2392.
- [62] R. Liu, A. Zhang, J. Tang, J. Tian, W. Huang, J. Cai, C. Barrow, W. Yang, J. Liu, *Chem. Eur. J.* **2019**, *25*, 5547–5554.
- [63] G. M. Suppes, C. G. Cameron, M. S. Freund, *J. Electrochem. Soc.* **2010**, *157*, A1030.
- [64] Y. Dong, L. Chen, W. Chen, X. Zheng, X. Wang, E. Wang, *Chem. Asian J.* **2018**, *13*, 3304–3313.
- [65] A. Anandan Vannathan, P. R. Chandewar, D. Shee, S. Sankar Mal, *J. Electroanal. Chem.* **2022**, *904*, 115856.

Manuscript received: March 6, 2022

Revised manuscript received: April 11, 2022

Accepted manuscript online: April 14, 2022

Version of record online: May 5, 2022